

# Dynamic molecular pockets on diffusion channel for efficient production of polymer-grade propylene

Dan Li (✉ [Danli@jnu.edu.cn](mailto:Danli@jnu.edu.cn))

Jinan University <https://orcid.org/0000-0002-4936-4599>

Heng Zeng

Jinan University

Ting Wang

Jinan University

Mo Xie

Jinan University

Rong-Jia Wei

Jinan University

Xiao-Jing Xie

Jinan University

Yifang Zhao

Jinan University

Weigang Lu

Jinan University <https://orcid.org/0000-0001-9751-8241>

---

Physical Sciences - Article

**Keywords:** polymer-grade propylene, sieving materials

**Posted Date:** February 15th, 2021

**DOI:** <https://doi.org/10.21203/rs.3.rs-222860/v1>

**License:**  This work is licensed under a Creative Commons Attribution 4.0 International License.

[Read Full License](#)

---

# Dynamic molecular pockets on diffusion channel for efficient production of polymer-grade propylene

Size-based molecular sieving works well for rigid molecules with complete exclusion of larger ones, yet interaction-induced molecular sieving may offer unusual separation capability for molecules with matching physicochemical properties. Here we report a MOF material (XXU-3) featuring one-dimension channels with embedded molecular pockets opening to  $C_3H_6$  and  $C_3H_8$  at substantially different pressures. The dynamic nature of the pockets is revealed by single-crystal-to-single-crystal transformation upon exposure of the activated XXU-3 to  $C_3H_6$  or  $C_3H_8$  atmosphere. Breakthrough experiments demonstrate that XXU-3 is not only capable of separating  $C_3H_6$  from  $C_3H_8$  with record-high  $C_3H_6$  productivity, but also the first MOF material realizing polymer-grade  $C_3H_6$  production in a single adsorption-desorption cycle from an equimolar  $C_3H_6/C_3H_8$  mixture. The underlying separation mechanism, namely orthogonal-array dynamic molecular sieving, is an exemplary strategy for both large separation capacity and fast adsorption-desorption kinetics. This work presents an ideal design for next-generation sieving materials and it holds great potential for applications in adsorptive separation.

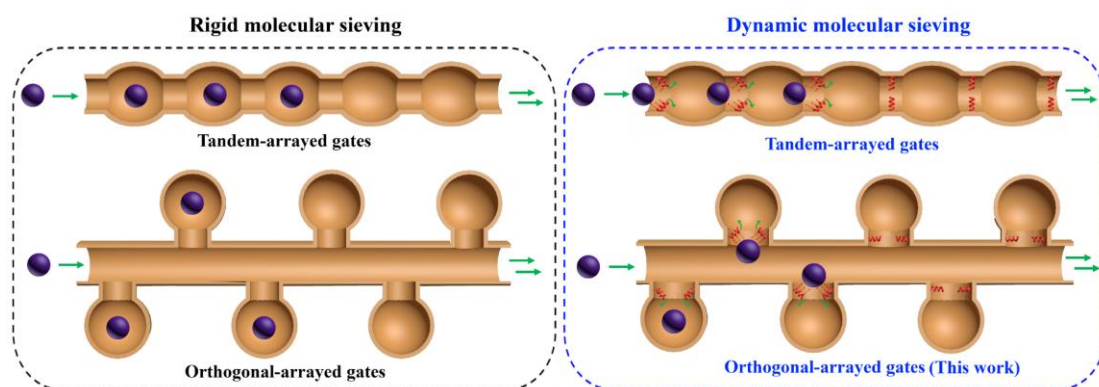
---

Propylene ( $C_3H_6$ ) is one of the most important feedstocks for polymer production in the petrochemical industry, with a projection of exceeding 130 million metric tons in 2023 worldwide<sup>1</sup>. Steam cracking of propane ( $C_3H_8$ ) and fluid catalytic cracking of gaseous oils are two commonly applied industrial processes for manufacturing  $C_3H_6$ , yet neither of them could produce polymer-grade  $C_3H_6$  ( $\geq 99.5\%$  pure)<sup>2-4</sup>. Prior to polymerization, cryogenic distillation is utilized to remove  $C_3H_8$  and other residues in the crude cracking products. This process, however, is extremely energy demanding primarily due to the operation of the multistage ultra-low-temperature refrigeration system (183 ~ 233 K)<sup>5</sup>, as  $C_3H_6$  and  $C_3H_8$  have close and low boiling points<sup>6</sup>.

Adsorption-based separation has been well established as an energy-efficient technology. It is deemed promising to replace the traditional cryogenic distillation and mitigate the high energy cost<sup>7-9</sup>. As an emerging class of crystalline solids constructed from metal nodes and organic linkers, metal-organic frameworks (MOFs) stand out for their precise control of structures and functions on a molecular level<sup>10-15</sup>. Through the careful tuning of pore environments, MOF materials have been demonstrated to be able to effectively distinguish guest molecules even for their slightest difference in polarizability, size, or shape<sup>16-26</sup>. One prominent feature of MOFs is their potential to incorporate high-density open metal sites (OMSs), which have been extensively studied for separating light alkenes from their saturated counterparts owing to the formation of metal  $\pi$ -complexation. However, OMSs alone would probably be insufficient to produce high-purity alkenes in one adsorption-desorption cycle, as they also interact with alkanes through polarization to some extent, not to mention their ability to form  $\pi$ -complexation could be substantially dampened in the presence of moisture. Many researchers are now resorting to another prominent feature of MOFs, i.e. tailor-made pore sizes and shapes, to boost the adsorption selectivity through the molecular sieving mechanism.

MOFs with narrow apertures appear to be functioning as size-based molecular sieves, taking up small-sized molecules while excluding the large-sized ones. Intuitively, the co-adsorption could

be minimized and selectivity maximized in such MOF materials, on condition that the aperture dimension is right in between the sizes of gas molecules to be separated<sup>27,28</sup>. For example, by employing a shorter organic linker of 4,4'-azopyridine (9.0 Å) instead of 4,4'-dipyridylacetylene (9.6 Å) in SIFSIX-2-Cu-i, an ideal C<sub>2</sub>H<sub>2</sub> molecular sieve SIFSIX-14-Cu-i (also termed as UTSA-200)<sup>29</sup> was constructed with a reduced pore size of 3.4 Å, falling right in between the kinetic diameters of C<sub>2</sub>H<sub>2</sub> (3.3 Å) and C<sub>2</sub>H<sub>4</sub> (4.2 Å). As a result, it displayed nearly perfect C<sub>2</sub>H<sub>2</sub>/C<sub>2</sub>H<sub>4</sub> selectivity by only taking up C<sub>2</sub>H<sub>2</sub>. Yet the tandem array of rigid apertures along one-dimension (1D) channel is a double-edged sword, on one hand, the high selectivity could be achieved by excluding the large-sized molecules; on the other hand, the equilibrium would be difficult to reach as the matching-sized molecules have to bump through many apertures, leading to slow adsorption-desorption kinetics and thus less energy efficiency. To alleviate the suppressed kinetics, a better design is to furnish the apertures on the channel surface instead of along the diffusion channel. Such a layout, namely orthogonal-array molecular sieving, is exemplified in the MOF material UTSA-100, which was demonstrated superior performance in removing C<sub>2</sub>H<sub>2</sub> from a C<sub>2</sub>H<sub>2</sub>/C<sub>2</sub>H<sub>4</sub> mixture with high efficiency<sup>30</sup>.



**Scheme 1.** Schematic representation of different molecular sieving mechanisms in MOF systems.

Size-based molecular sieving works well for rigid molecules. Yet it can be anticipated that this approach will be less powerful for molecules with more flexibility. In such a case, interaction-induced molecular sieving (dynamic molecular sieving) would be advantageous if the molecules to be separated could induce gate opening at different pressures. In other words, the apertures preferentially interact with and take up guest molecules of particular physicochemical properties, not necessarily the small-sized ones. A good MOF example that fits right in this category is MAF-41 developed by Zhang and co-workers<sup>31</sup>. This flexible MOF material exhibits adsorption of styrene but no adsorption of toluene or benzene. The latter two, although smaller in size, do not have sufficient adsorption energy to open the cavity. Clearly, framework flexibility has unique advantages in adsorptive separation if properly controlled. So far the rational design and control of local flexibility in the MOF framework for dynamic molecular sieving remain difficult and challenging. Some representative works are mesh-adjustable molecular sieve by Zhou<sup>32</sup>, chemical-triggered pore adaptation by Rosseinsky<sup>33</sup>, and temperature-responsive pore aperture by Kitagawa<sup>34</sup>, *etc.* A rare example in C<sub>3</sub>H<sub>6</sub>/C<sub>3</sub>H<sub>8</sub> separation is the fluorinated MOF NbOFFIVE-1-Ni (also termed as KAUST-7)<sup>16</sup>, in which the dynamic nature of the pore aperture is presumably associated with the rotation and tilting of the pyrazine rings. The internal cavities of KAUST-7 along the 1D channel are

interconnected by dynamic apertures that serve as sieving sites for C<sub>3</sub>H<sub>6</sub>. Nevertheless, as a tandem-array molecular sieve, the low kinetics and associated energy penalty seem inevitable given that gas molecules have to push through many independent gates in order to get through. Thus, orthogonal-array dynamic molecular sieving (**Scheme 1**) would be an ideal design to achieve not only large selectivity but also fast kinetics. Herein we report such a MOF (XXU-3, XXU = XX University) featuring dynamic molecular pockets opening to 1D diffusion channel. The pockets function as interaction-induced sieving sites for desired molecules to dock during the adsorption stage, while the 1D channels facilitate fast adsorption-desorption diffusion. Single- and mixed-component gas adsorption data suggest the pockets open to C<sub>3</sub>H<sub>6</sub> and C<sub>3</sub>H<sub>8</sub> at substantially different partial pressures. Breakthrough experiments reveal that XXU-3 is capable of efficiently separating C<sub>3</sub>H<sub>6</sub> from C<sub>3</sub>H<sub>8</sub> from an equimolar C<sub>3</sub>H<sub>6</sub>/C<sub>3</sub>H<sub>8</sub> mixture with record-high C<sub>3</sub>H<sub>6</sub> productivity, and it is the first MOF material realizing polymer-grade C<sub>3</sub>H<sub>6</sub> production in a single adsorption-desorption cycle, which was previously achieved by Y-abtc, but from a C<sub>3</sub>H<sub>6</sub>/C<sub>3</sub>H<sub>8</sub> mixture of 5/95<sup>17</sup>.

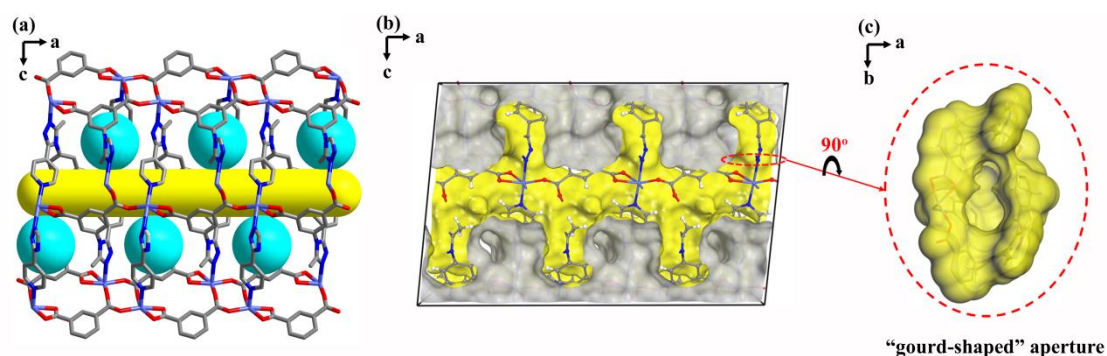


**Fig. 1. Crystal structure of XXU-3.** (a) Pore structure viewed along the *b* axis showing molecular pockets (turquoise) and one-dimension channel (yellow). (b) Cross-sectional view of Connolly surface of the void in (a), where a probe radius of 0.8 Å was used to visualize the molecular pockets opening to the one-dimension channel. (c) Close-up view of the “gourd-shaped” aperture connecting the pocket to the channel. Color code: light blue, Co; red, O; blue, N; white, H; grey, C atoms. H atom is omitted in (a) for clarity.

### Synthesis and structural analysis

Solvothermal reaction of 5-(3-methyl-5-(pyridin-4-yl)-4*H*-1,2,4-triazol-4-yl)-1,3-benzenedicarboxylic acid (H<sub>2</sub>MPTBDC, **Supplementary Fig. 1**) and Co (II) chloride in a mixture of dimethylacetamide/methanol (*v/v* = 1:1) at 120 °C for 12 h yielded light purple crystals of XXU-3. Single-crystal X-ray diffraction (SCXRD) reveals that the as-synthesized XXU-3 crystallizes in the monoclinic space group *P*2<sub>1</sub>/*c* with an asymmetric unit consisting of one linker and one Co<sup>2+</sup> ion (**Supplementary Fig. 2**). Each Co (II) center is octahedrally coordinated by four carboxylate oxygen atoms from three MPTBDC linkers and two nitrogen atoms from two other linkers (**Supplementary Fig. 3**), translating into a three-dimensional (3D) porous network (**Figs. 1a-c**, and **Supplementary Fig. 4**) with a calculated void ratio of 0.20 by PLATON software (guest omitted).

The phase purity of bulk XXU-3 was analyzed with powder X-ray diffraction (PXRD), and its diffraction pattern is in good agreement with the simulated one from single-crystal data (**Supplementary Fig. 5**). XXU-3 is thermally stable up to ~ 400 °C, as evidenced by thermogravimetric analysis (TGA) and variable-temperature PXRD analysis (**Supplementary Fig. 6**). To explore the permanent porosity, the as-synthesized XXU-3 was solvent-exchanged with

methanol, followed by activation at 150 °C under a high vacuum for 24 h to afford the desolvated XXU-3 (XXU-3a). PXRD was first employed to attest to the retention of the framework of XXU-3a (**Supplementary Fig. 7**). Then Ar adsorption/desorption isotherms were measured at 87 K (**Fig. 2a**), showing a type-I sorption behavior with saturated adsorption of 198 cm<sup>3</sup> (STP) g<sup>-1</sup> at 1 bar. Based on its Ar adsorption isotherm, XXU-3a was calculated to have a Brunauer–Emmett–Teller (BET) surface area of 588 m<sup>2</sup> g<sup>-1</sup>, an extremely narrow pore size distribution centered at 5.6 Å, and a total pore volume of 0.27 cm<sup>3</sup> g<sup>-1</sup>. All these data are consistent with the theoretical values calculated from the crystal structure, further suggesting the retention of the framework after activation.

XXU-3a retains high-quality crystallinity and the SCXRD analysis reveals a 1D channel of *ca.* 4.5 Å × 5.3 Å dimension along the crystallographic *a*-axis (**Supplementary Fig. 4**) with a cross-sectional area of *ca.* 23.85 Å<sup>2</sup>, which is substantially larger than the minimum cross-sections of C<sub>3</sub>H<sub>6</sub> (19.34 Å<sup>2</sup>) and C<sub>3</sub>H<sub>8</sub> (18.17 Å<sup>2</sup>) (**Supplementary Fig. 8**). In addition, molecular-sized pockets are lined up on both sides of the 1D channel and open to the channel through a “gourd-shaped” aperture of *ca.* 3.7 Å in size along the *a*-axis (**Supplementary Fig. 9**). From a kinetics point of view, the “gourd-shaped” aperture seems impossible for C<sub>3</sub>H<sub>6</sub> (kinetic diameter *ca.* 4.0 Å) and C<sub>3</sub>H<sub>8</sub> (kinetic diameter *ca.* 4.3 Å)<sup>35</sup> to go through. Nevertheless, the aromatic rings on MPTBDC linker were observed flexibility in tilting and rotation through *in-situ* variable-temperature SCXRD studies on XXU-3a (**Supplementary Fig. 10**), indicating the potential of opening up the “gourd-shaped” aperture to facilitate the admission of right-sized guest molecules such as C<sub>3</sub>H<sub>6</sub> and C<sub>3</sub>H<sub>8</sub> into the pockets.

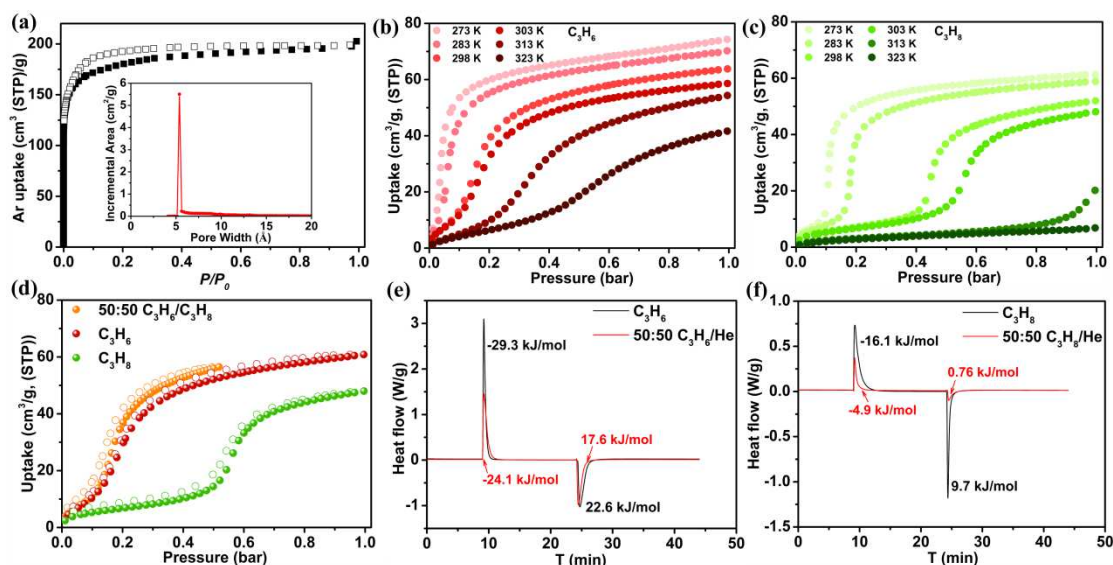


**Fig. 2. Gas sorption properties and DSC profiles.** (a) Low-pressure Ar adsorption/desorption isotherms of XXU-3a at 87 K. (inset) calculated pore-size distribution of XXU-3a based on the adsorption branch. (b) C<sub>3</sub>H<sub>6</sub> adsorption isotherms of XXU-3a at different temperatures. (c) C<sub>3</sub>H<sub>8</sub> adsorption isotherms of XXU-3a at different temperatures. (d) Pure C<sub>3</sub>H<sub>8</sub> (green), pure C<sub>3</sub>H<sub>6</sub> (red), and an equimolar mixture of C<sub>3</sub>H<sub>6</sub>/C<sub>3</sub>H<sub>8</sub> (orange) adsorption/desorption isotherms of XXU-3a at 303 K. For the equimolar mixture, the x-axis is partial pressure of C<sub>3</sub>H<sub>6</sub>. (e) Differential scanning calorimetry of C<sub>3</sub>H<sub>6</sub> and 50/50 C<sub>3</sub>H<sub>6</sub>/He adsorption and desorption on XXU-3a at 303 K and 1 bar. (f) Differential scanning calorimetry of C<sub>3</sub>H<sub>8</sub> and 50/50 C<sub>3</sub>H<sub>8</sub>/He adsorption and desorption on XXU-3a at 303 K and 1 bar. In (e) and (f), the adsorption was carried out under C<sub>3</sub>H<sub>6</sub>, C<sub>3</sub>H<sub>8</sub>, or 50/50 mixed-component (C<sub>3</sub>H<sub>6</sub>/He and

C<sub>3</sub>H<sub>8</sub>/He) at a flow rate of 5.0 mL min<sup>-1</sup>. The desorption was carried out under helium at a flow rate of 5.0 mL min<sup>-1</sup> starting at 15-min time point.

### Gas adsorption and kinetic studies

Pure-component C<sub>3</sub>H<sub>6</sub> and C<sub>3</sub>H<sub>8</sub> adsorption/desorption isotherms were collected for XXU-3a at different temperatures. As shown in **Figs. 2b** and **c**, both C<sub>3</sub>H<sub>6</sub> and C<sub>3</sub>H<sub>8</sub> display stepwise adsorptions. As the temperature increases, the sharp adsorption steps gradually fade away, and the initiation of those steps shifts toward higher pressures. Such a stepwise adsorption isotherm may be attributed to the guest-induced gate-opening behavior, as frequently reported in flexible MOFs<sup>36-39</sup>. Interestingly, the gate-opening pressure for C<sub>3</sub>H<sub>8</sub> is approximately 5 times higher than that for C<sub>3</sub>H<sub>6</sub> at 303 K, suggesting a high selectivity for C<sub>3</sub>H<sub>6</sub> over C<sub>3</sub>H<sub>8</sub> in the pocket. While in the low-pressure region before gate opening (e.g., 0.1 bar), a small amount of C<sub>3</sub>H<sub>8</sub> (0.24 mmol g<sup>-1</sup>) can be adsorbed, and the value is 0.46 mmol g<sup>-1</sup> for C<sub>3</sub>H<sub>6</sub> at 303 K, suggesting a moderate selectivity for C<sub>3</sub>H<sub>6</sub> over C<sub>3</sub>H<sub>8</sub> in the channel (**Supplementary Figs. 11**). The C<sub>3</sub>H<sub>6</sub> uptake in XXU-3a can reach 58.6 cm<sup>3</sup> g<sup>-1</sup> (2.6 mmol g<sup>-1</sup>) at 1 bar and 303 K, higher than those benchmark C<sub>3</sub>H<sub>6</sub>/C<sub>3</sub>H<sub>8</sub> molecular sieves, such as zeolite 4A (1.5 ~ 2 mmol g<sup>-1</sup>)<sup>40,41</sup>, KAUST-7<sup>16</sup> (1.4 mmol g<sup>-1</sup>), Co-gallate (1.8 mmol g<sup>-1</sup>)<sup>42</sup> and Y-abtc<sup>17</sup> (2.0 mmol g<sup>-1</sup>) at 1 bar and 298 K. Remarkably, based on the adsorbed C<sub>3</sub>H<sub>6</sub> and the calculated pore volume, the density of C<sub>3</sub>H<sub>6</sub> inside XXU-3a is estimated to be 404 g L<sup>-1</sup> at 303 K and 1 bar, which is more than 230 times higher than the density of gaseous C<sub>3</sub>H<sub>6</sub> (1.707 g L<sup>-1</sup>) under similar conditions, and close to the density of liquid C<sub>3</sub>H<sub>6</sub> (608 g L<sup>-1</sup>) at 225 K and 1 bar, demonstrating a highly efficient packing of C<sub>3</sub>H<sub>6</sub> molecules inside XXU-3a. Further, the adsorption/desorption isotherms of both C<sub>3</sub>H<sub>6</sub> and C<sub>3</sub>H<sub>8</sub> are reversible and exhibit no obvious hysteresis (**Fig. 2d**); the continuous adsorption/desorption measurement on XXU-3a at 303 K shows no loss in C<sub>3</sub>H<sub>6</sub> adsorption capacity over 10 cycles (**Supplementary Figs. 12 and 13**), suggesting no elevated temperature required for regeneration.

To quantify the binding affinity toward C<sub>3</sub>H<sub>6</sub> and C<sub>3</sub>H<sub>8</sub>, coverage-dependent adsorption enthalpy ( $Q_{st}$ ) was calculated (**Supplementary Figs. 14 and 15**) from their respective adsorption isotherms at 273, 283, and 298 K by the virial fitting method. The adsorption enthalpy of XXU-3a for C<sub>3</sub>H<sub>6</sub> and C<sub>3</sub>H<sub>8</sub> were calculated to be 38.9 kJ/mol and 34.6 kJ/mol, respectively, at zero coverage. However, the data seem inconsistent at higher pressures (**Supplementary Fig. 16**). We suspect the virial model may not accurately reflect the adsorption behavior for MOF materials with stepwise adsorption isotherms. Thus, we performed differential scanning calorimetry of C<sub>3</sub>H<sub>6</sub> and C<sub>3</sub>H<sub>8</sub> adsorption and desorption on XXU-3a at 303 K and 1 bar to obtain the experimental adsorption/desorption enthalpy. As shown in **Figs. 2e-f** and **Supplementary Fig. 18**, the adsorption enthalpy of XXU-3a for C<sub>3</sub>H<sub>8</sub> and C<sub>3</sub>H<sub>6</sub> were found to be 16.1 kJ mol<sup>-1</sup> and 29.3 kJ mol<sup>-1</sup>, respectively. The subsequent desorption enthalpy upon helium flow was found to be 11.3 kJ mol<sup>-1</sup> and 22.6 kJ mol<sup>-1</sup>, respectively. Note that the adsorption enthalpy value for C<sub>3</sub>H<sub>6</sub> is markedly lower than many of the leading C<sub>3</sub>H<sub>6</sub>-selective sorbents (**Supplementary Fig. 17** and **Table 5**), such as Fe<sub>2</sub>(m-dobdc) (65 kJ mol<sup>-1</sup>), KAUST-7 (57.4 kJ mol<sup>-1</sup>), Co-gallate (41.0 kJ mol<sup>-1</sup>), and Y-abtc (50 kJ mol<sup>-1</sup>). Such a low adsorption enthalpy of XXU-3a for C<sub>3</sub>H<sub>6</sub> is consistent with the adsorption/desorption cycling experiment, further corroborating the potential of easy regeneration for XXU-3a in C<sub>3</sub>H<sub>6</sub>/C<sub>3</sub>H<sub>8</sub> separation. It is worth mentioning that elevated temperatures could cause C<sub>3</sub>H<sub>6</sub> oligomerization/polymerization in a confined space<sup>43</sup>.

Arguably, C<sub>3</sub>H<sub>6</sub>-induced framework transformation in flexible MOFs could enable subsequent

simultaneous uptake of C<sub>3</sub>H<sub>8</sub> molecules, compromising the C<sub>3</sub>H<sub>6</sub>/C<sub>3</sub>H<sub>8</sub> separation efficiency. To investigate the potential co-adsorption of C<sub>3</sub>H<sub>8</sub> after C<sub>3</sub>H<sub>6</sub>-induced gate-opening in XXU-3a, a mixed-component (C<sub>3</sub>H<sub>6</sub>/C<sub>3</sub>H<sub>8</sub>, 50/50, mol/mol) adsorption experiment was performed under similar conditions to those used in single-component adsorption experiments. The mixed-gas adsorption isotherm (partial pressure of C<sub>3</sub>H<sub>6</sub> up to 0.5 bar) almost overlaid with the pure C<sub>3</sub>H<sub>6</sub> adsorption isotherm (**Fig. 2d**), suggesting preferential adsorption of C<sub>3</sub>H<sub>6</sub> over C<sub>3</sub>H<sub>8</sub> for an equimolar mixture. Differential scanning calorimetry of 50/50 mixed-component (C<sub>3</sub>H<sub>6</sub>/He, C<sub>3</sub>H<sub>8</sub>/He, and C<sub>3</sub>H<sub>6</sub>/C<sub>3</sub>H<sub>8</sub>) was performed at 303 K (**Figs. 2e-f** and **Supplementary Fig. 19**). The small heat flux peaks in the case of 50/50 C<sub>3</sub>H<sub>8</sub>/He indicate a rather weak interaction of XXU-3a with C<sub>3</sub>H<sub>8</sub> at 0.5 bar, corroborating the preferential adsorption of C<sub>3</sub>H<sub>6</sub> over C<sub>3</sub>H<sub>8</sub> for an equimolar mixture on XXU-3a. The ideal adsorbed solution theory (IAST)<sup>44</sup> was applied to calculate the adsorption selectivity for an equimolar mixture of C<sub>3</sub>H<sub>6</sub>/C<sub>3</sub>H<sub>8</sub>, and an exceptionally high C<sub>3</sub>H<sub>6</sub> over C<sub>3</sub>H<sub>8</sub> selectivity (513) was found for XXU-3a (**Supplementary Figs. 20-22**), far superior to many C<sub>3</sub>H<sub>6</sub>-selective materials reported, such as CoMOF-74 (46), Fe<sub>2</sub>(m-dobdc) (55), ITQ-12 (15), CPL-1 (2.08), and NJU-Bai8 (43.2), *etc* (**Supplementary Table 5**). Compared to MOFs with global flexibility, MOFs with local flexibility appear to be more promising in minimizing co-adsorption and realizing high selectivity due to the independence of gate opening. Nevertheless, it should be pointed out that IAST selectivity is calculated based on fitting single-component adsorption isotherm to a selected model, however, models for stepwise adsorption in flexible MOFs are still lacking; therefore, the resulting IAST selectivity may not accurately reflect its separation potential.

The overall kinetic behavior for a particular guest is governed not only by its binding affinity (adsorption enthalpy) but also its diffusion rate within the host<sup>45</sup>. From a structure point of view, molecular sieving with orthogonally arrayed apertures, as in XXU-3a, is intrinsically a better design to realize fast kinetics, given each gas molecule only has to push through one aperture in an adsorption/desorption cycle. To verify its kinetic advantage, time-dependent adsorption/desorption isotherms of C<sub>3</sub>H<sub>6</sub> on XXU-3a were recorded at 303 K, along with two benchmark molecular sieving materials with tandemly arrayed apertures, KAUST-7 and Y-abtc (**Supplementary Fig. 26**). Remarkable differences in their diffusion rates are observed, and C<sub>3</sub>H<sub>6</sub> diffuses much faster in XXU-3a than the other two materials both in adsorption and desorption stages. To further quantify the difference, the diffusion rate constant ( $D/r^2$ ) was calculated to be 2.94E-003 for XXU-3a, which is more than one order of magnitude higher than KAUST-7 (8.66E-004,) and Y-abtc (7.64E-005) (**Supplementary Fig. 23**).

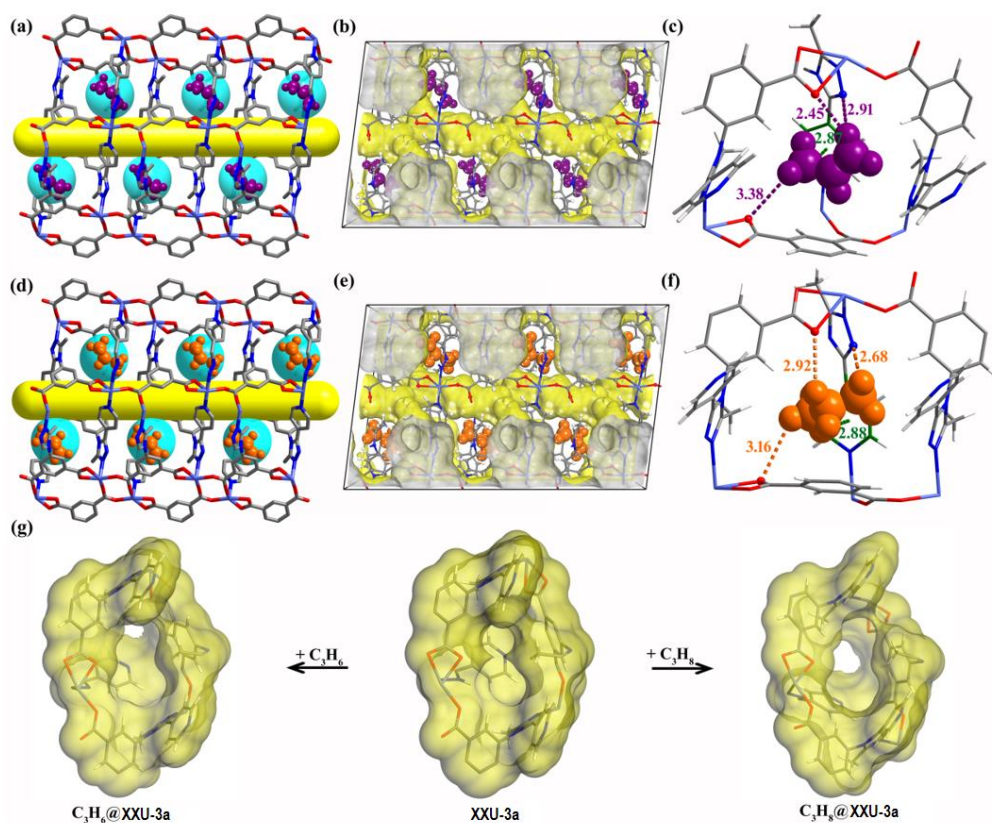


**Fig. 3. Binding sites and dynamic gate-opening.** (a) Crystal structure of  $C_3H_6@XXU-3a$  viewed along the  $b$  axis highlighting the pocket-occupying  $C_3H_6$  molecules. (b) Connolly surface representation of  $C_3H_6@XXU-3a$  along the  $b$  axis with the adsorbed  $C_3H_6$  molecules. (c) Close-up view of  $C_3H_6$  in the single crystal of  $C_3H_6@XXU-3a$ , showing multiple interactions with surrounding linkers on the pocket.  $C_3H_6$  molecules are shown in a space-filling model depicted in violet, and distances are in Å. (d) Crystal structure of  $C_3H_8@XXU-3a$  viewed along the  $b$  axis highlighting the pocket-occupying  $C_3H_8$  molecules. (e) Connolly surface representation of  $C_3H_8@XXU-3a$  along the  $b$  axis with the adsorbed  $C_3H_8$  molecules. (f) Close-up view of  $C_3H_8$  in the single crystal of  $C_3H_8@XXU-3a$ , showing multiple interactions with surrounding organic linkers on the pocket,  $C_3H_8$  molecules are shown in a space-filling model depicted in orange, and distances are in Å. (g) Connolly surface comparison to illustrate the opening up of the “gourd-shaped” aperture along with the adsorption of  $C_3H_6$  or  $C_3H_8$ .  $C_3H_8$  and  $C_3H_6$  were omitted for clarity. Color code: light blue, red, blue, white, and grey nodes represent Co, O, N, H, and C atoms, respectively. H atom is omitted in (a) and (d) for clarity.

### Dynamic sieving mechanism and breakthrough experiments

To understand the gate-opening behavior of XXU-3a, single-crystal-to-single-crystal transformation was studied. First, an XXU-3a crystal of good quality was picked and its single crystal data was collected at 150 K. Then, the same crystal was exposed to the  $C_3H_6$  atmosphere at room temperature for 3 h and its single crystal data was collected again at 150 K. From the analysis of the crystal structures of XXU-3a and  $C_3H_6@XXU-3a$ , the pockets are confirmed to be the preferential binding sites for  $C_3H_6$  molecules (**Figs. 3a** and **b**), and four  $C_3H_6$  molecules are found per unit cell, which is consistent with the measured  $C_3H_6$  adsorption capacity at 1 bar and 298 K. Compared with XXU-3a, the unit cell of  $C_3H_6@XXU-3a$  exhibits some deformation. The organic linker in  $C_3H_6@XXU-3a$  adopts a slightly different conformation through aromatic rings tilting and

rotation in response to the adsorbed C<sub>3</sub>H<sub>6</sub> molecules in the pockets (**Supplementary Figs. 27 and 28**). As a result, the unit cell volume is expanded by 6 % to 1963.72 Å<sup>3</sup>. Specifically, multiple interactions are found between the C<sub>3</sub>H<sub>6</sub> molecule and surrounding organic linkers on the pocket, including two weak interactions with two carboxylate oxygen atoms (2.45 Å and 3.38 Å), one weak interaction with a triazole nitrogen atom (2.91 Å), and one C–H···π interaction with pyridine ring (2.87 Å) (**Fig. 3c**). For comparison, we managed to obtain the crystal structure of C<sub>3</sub>H<sub>8</sub>@XXU-3a at 100 K and found the pockets are also the preferential binding sites for C<sub>3</sub>H<sub>8</sub> molecules (**Figs. 3d and 3e**). Not surprisingly, the C<sub>3</sub>H<sub>8</sub> molecules are interacting with surrounding organic linkers on the pocket, including two weak interactions with two carboxylate oxygen atoms (2.92 Å and 3.16 Å), one weak interaction with a triazole nitrogen atom (2.68 Å), and one C–H···π interaction with the pyridine ring (2.88 Å) (**Fig. 3f**). Connolly surface comparison of the “gourd-shaped” apertures in XXU-3a (3.7 Å), C<sub>3</sub>H<sub>8</sub>@XXU-3a (4.4 Å), and C<sub>3</sub>H<sub>6</sub>@XXU-3a (4.4 Å) indicate the opening up of the aperture along with the adsorption of C<sub>3</sub>H<sub>6</sub> or C<sub>3</sub>H<sub>8</sub> (**Fig. 3g**).

Many efforts were devoted to gas-loaded crystal structures, yet only at low temperatures did we successfully collect C<sub>3</sub>H<sub>6</sub>@XXU-3a and C<sub>3</sub>H<sub>8</sub>@XXU-3a crystal data. To further quantify the binding affinity of C<sub>3</sub>H<sub>6</sub> and C<sub>3</sub>H<sub>8</sub> in XXU-3a at room temperature, in the work reported here we performed density functional theory (DFT) calculations by employing Perdew-Burke-Ernzerhof (PBE) functional<sup>46</sup>. In the optimized host–guest structures at room temperature, the binding configurations for both C<sub>3</sub>H<sub>6</sub> and C<sub>3</sub>H<sub>8</sub> (**Supplementary Fig. 29**) are in good agreement with C<sub>3</sub>H<sub>6</sub>@XXU-3a and C<sub>3</sub>H<sub>8</sub>@XXU-3a structures determined by SCXRD at low temperatures. The static binding energy  $\Delta E$  ( $\Delta E = E_{\text{MOF+gas}} - E_{\text{MOF}} - E_{\text{gas}}$ ) at room temperature was thus calculated to be –19.96 and –16.52 kJ mol<sup>-1</sup> for C<sub>3</sub>H<sub>6</sub> and C<sub>3</sub>H<sub>8</sub>, respectively. The appreciable difference in binding energy (3.44 kJ mol<sup>-1</sup>) could be attributed to the stronger C–H···O and C–H···N interactions with C<sub>3</sub>H<sub>6</sub> than C<sub>3</sub>H<sub>8</sub> (**Supplementary Fig. 29**). Subsequently, C<sub>3</sub>H<sub>6</sub> and C<sub>3</sub>H<sub>8</sub> kinetic adsorption studies were carried out on XXU-3a and found that it is much faster for C<sub>3</sub>H<sub>6</sub> to reach adsorption saturation plateau than C<sub>3</sub>H<sub>8</sub> (**Supplementary Fig. 24**). Furthermore, the diffusion rate constant was calculated to be 2.94E-003, which is more than one order of magnitude higher than that for C<sub>3</sub>H<sub>8</sub> (4.53E-004) (**Supplementary Fig. 24**). Thus, we conclude that the adsorption of C<sub>3</sub>H<sub>6</sub> is both favored by thermodynamics and kinetics, leading to high C<sub>3</sub>H<sub>6</sub>/C<sub>3</sub>H<sub>8</sub> selectivity.

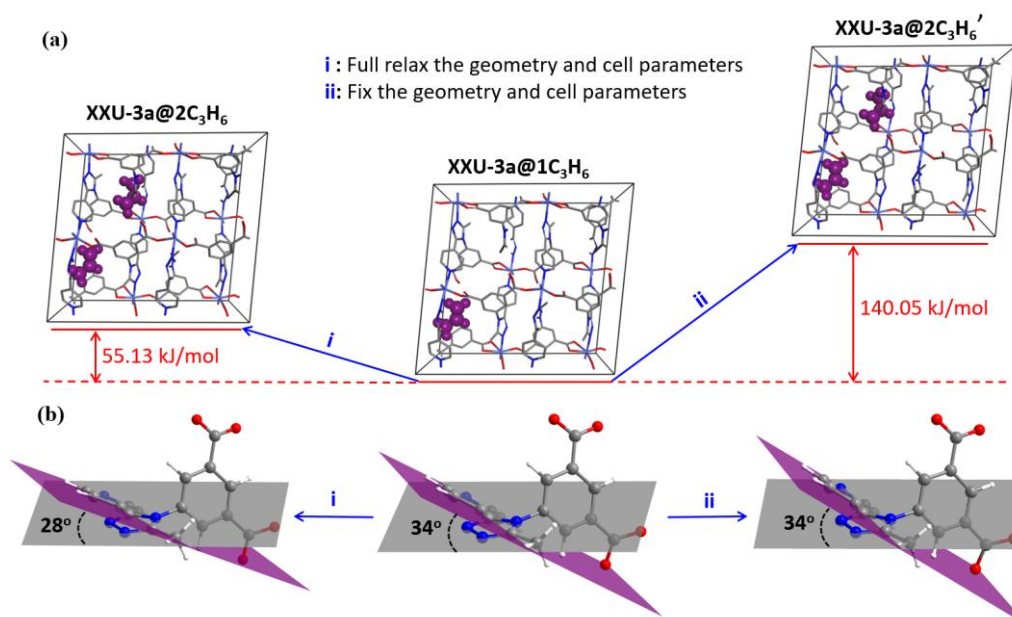


**Fig. 4. DFT calculations.** (a) Geometry optimization by density functional theory (DFT) for (i)  $XXU-3a@2C_3H_6$ , full relax the geometry and cell parameters; and (ii)  $XXU-3a@2C_3H_6'$ , fix the geometry and cell parameters. (b) The rotation of the dihedral angle of the pyridine plane and triazole plane. Color code: light blue, red, blue, white, and grey represent Co, O, N, H, and C atoms, respectively. H atom is omitted in (a) for clarity.

To further look into plausible adsorption mechanism for XXU-3a, specifically whether all the pockets open in a cooperative manner or each pocket has to further rearrange in order to accommodate  $C_3H_6$ , we performed DFT simulation on XXU-3a by loading  $C_3H_6$  one by one. As illustrated in **Fig. 4a**, the first  $C_3H_6$  was put in the bottom left pocket of XXU-3a and the structure ( $XXU-3a@1C_3H_6$ ) was optimized by DFT calculations with all-atom positions and unit cell parameters allowed to vary. Starting from the optimized  $XXU-3a@1C_3H_6$ , the second  $C_3H_6$  was put in the top left pocket and the structure ( $XXU-3a@2C_3H_6$ ) was optimized by DFT calculations under two different conditions: (i) full relax the geometry and cell parameters (all-atom positions and unit cell parameters allowed to vary); and (ii) fix the geometry and cell parameters (all-atom positions and unit cell parameters not allowed to vary). Upon the completion of optimization, the rotation of the pyridine ring was observed in (i) with a dihedral angle of the pyridine plane and triazole plane rotating from  $34^\circ$  to  $28^\circ$  (**Fig. 4b**). The energy difference ( $\Delta E = E_{XXU-3a@2C_3H_6} - E_{XXU-3a@1C_3H_6} - E_{C_3H_6}$ ) was calculated to be  $55.1 \text{ kJ mol}^{-1}$  and  $140.1 \text{ kJ mol}^{-1}$  for scenarios (i) and (ii), respectively. The large energy difference suggests further local rearrangement is energetically favored for the pocket to accommodate the second  $C_3H_6$ . Thus, a cooperative framework rearrangement may occur to some extent (unit cell volume expanded by 6 %), but itself alone would be energetically disfavored. The gate-opening adsorption behavior is likely due to a combination of global flexibility (cooperative framework rearrangement) and local flexibility (e.g., pyridine ring rotation); the latter seems to be the major contributor in the case of XXU-3a.

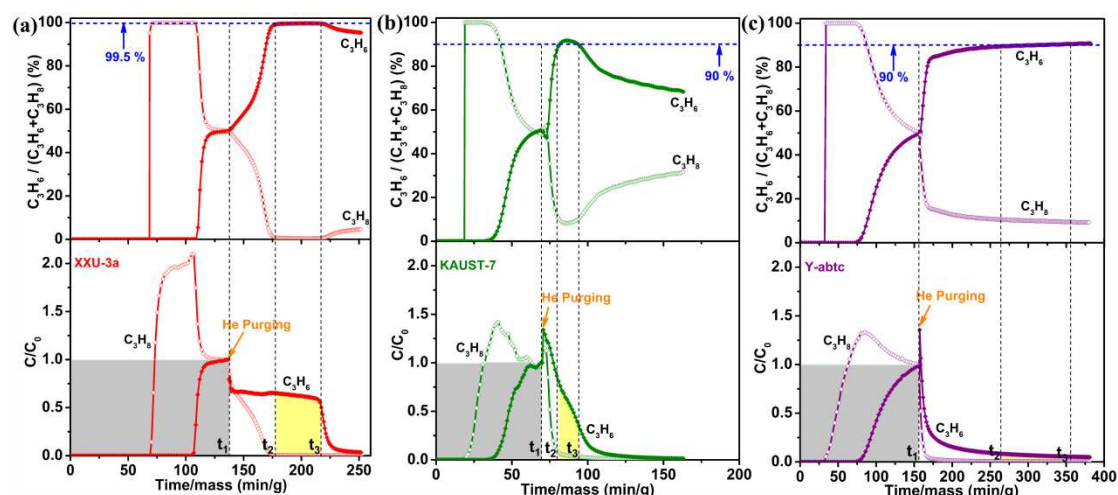


**Fig. 5. Breakthrough experiments.** Breakthrough curves of an equimolar mixture of  $C_3H_6/C_3H_8$  ( $1.0 \text{ mL min}^{-1}$ ) on XXU-3a, KAUST-7, and Y-abtc, followed by desorption curves under helium gas ( $10.0 \text{ mL min}^{-1}$ ) sweeping at 303 K.  $C_3H_8$  (open diamonds),  $C_3H_6$  (solid diamonds). For comparison, the x-axis is normalized to “time per gram adsorbents”. C and  $C_0$  are the concentrations of each gas at the outlet and inlet, respectively. Dashed blue lines highlight the gas composition at 99.5 % and 90 %, respectively. Grey area: mixed gas input. Yellow area:  $C_3H_6$  gas output.

The industrial production of  $C_3H_6$  by steam cracking usually contains 40 ~ 50 % of  $C_3H_8$ <sup>47</sup>. Although more than a few MOF materials have been demonstrated their outstanding performance in  $C_3H_6$  purification<sup>16,17</sup>, hardly any exhibits separation capability of producing polymer-grade  $C_3H_6$  from an equimolar  $C_3H_6/C_3H_8$  mixture in a single adsorption/desorption cycle. To evaluate the separation capacity of XXU-3a for  $C_3H_6/C_3H_8$  mixtures, dynamic column breakthrough experiments were conducted, in which an equimolar  $C_3H_6/C_3H_8$  mixture flowed over a packed column of XXU-3a sample (1.4 g) at a rate of  $1.0 \text{ mL min}^{-1}$  and 303 K (**Fig. 5a** and **Supplementary Fig. 30**). Breakthrough curves reveal that XXU-3a is capable of completely separating an equimolar  $C_3H_6/C_3H_8$  mixture into individual components. As shown in **Fig. 5a**,  $C_3H_8$  was eluted from the column first, and then the outlet  $C_3H_8$  gas quickly reached high-purity with no detectable  $C_3H_6$  (below the detection limit of the instrument, 0.01 %) (**Supplementary Fig. 31**); whereas  $C_3H_6$  was preferentially adsorbed by XXU-3a and breaking through the column after a substantial time lapse.

The excellent breakthrough performance of XXU-3a encouraged us to conduct desorption experiments for  $C_3H_6$  purity and productivity. For comparison, breakthrough experiments of an equimolar  $C_3H_6/C_3H_8$  mixture were also carried out over a packed column of KAUST-7 or Y-abtc under the same condition as for XXU-3a (**Figs. 5a-c**). Upon reaching breakthrough equilibrium, the captured gas in the column was purged by helium gas sweeping ( $10 \text{ mL min}^{-1}$ ) at 303 K, and the outlet gas was monitored by gas chromatography. The  $C_3H_6$  purity and productivity were estimated from their desorption curves (**Figs. 5a-c** and **Supplementary Fig. 32**) by using a calibration curve of  $C_3H_6$  flowrate vs. its peak area on gas chromatogram (**Supplementary Table 3** and **Figs. 33-39**). It turns out that 34.2 L of  $C_3H_6$  with over 99.5 % purity could be obtained from an equimolar  $C_3H_6/C_3H_8$  mixture for 1 kg of XXU-3a in a single adsorption-desorption cycle, the value was significantly higher than those for KAUST-7 (16.3 L with 90.0 % purity) and Y-abtc (1.3 L with 90.0 % purity), the two benchmark MOF materials with the best performance reported so far for  $C_3H_6/C_3H_8$  separation. For 100 g of  $C_3H_6/C_3H_8$  (50/50) mixed gas input, XXU-3a, KAUST-7, and

Y-abtc could produce 25.6 g (99.5 %), 22.8 g (90 %), and 0.8 g (90 %) of C<sub>3</sub>H<sub>6</sub>, respectively. These results demonstrate that XXU-3a is capable of efficiently producing C<sub>3</sub>H<sub>6</sub> with both record-high purity and productivity in a single adsorption-desorption cycle from an equimolar C<sub>3</sub>H<sub>6</sub>/C<sub>3</sub>H<sub>8</sub> mixture.

The initial slope of the desorption curve observed on XXU-3a is much lower, and it takes almost 40 min to start producing high-purity propylene, indicating co-adsorption of C<sub>3</sub>H<sub>6</sub>/C<sub>3</sub>H<sub>8</sub> on XXU-3a in the breakthrough experiment, which is consistent with the adsorption capacity estimated from the breakthrough curves (**Supplementary Figs. 40 and 41**). By integrating the corresponding areas on the breakthrough curves, the dynamic adsorption capacity of C<sub>3</sub>H<sub>6</sub> and C<sub>3</sub>H<sub>8</sub> upon breakthrough equilibrium were estimated to be 54.9 mL g<sup>-1</sup> and 18.7 mL g<sup>-1</sup>, respectively, (**Supplementary Figs. 40-41 and Table 4**). The co-adsorption of C<sub>3</sub>H<sub>6</sub>/C<sub>3</sub>H<sub>8</sub> could be attributed to the less selective adsorption sites such as channels and the interstices between particles. These were probably purged first during the desorption process, corresponding to the 40-min elution of a C<sub>3</sub>H<sub>6</sub>/C<sub>3</sub>H<sub>8</sub> mixture on the desorption curve, and then, C<sub>3</sub>H<sub>6</sub> in the pockets were subsequently purged, translating into the high-purity C<sub>3</sub>H<sub>6</sub>.

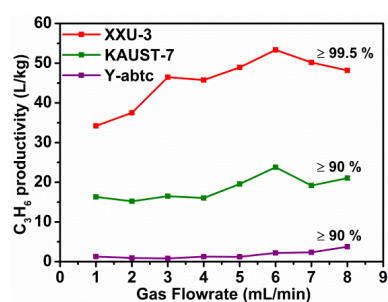


**Fig. 6. C<sub>3</sub>H<sub>6</sub> productivity and purity.** Comparison of C<sub>3</sub>H<sub>6</sub> productivity and purity estimated from the experimental breakthrough data of an equimolar C<sub>3</sub>H<sub>6</sub>/C<sub>3</sub>H<sub>8</sub> mixture on XXU-3a, KAUST-7, and Y-abtc at different flowrates.

To further highlight the practical industrial applications of XXU-3a as a solid adsorbent, we performed dynamic column breakthrough curves of an equimolar C<sub>3</sub>H<sub>6</sub>/C<sub>3</sub>H<sub>8</sub> mixture at higher flow rates (up to 8.0 mL min<sup>-1</sup>) on XXU-3a, KAUST-7, and Y-abtc. As shown in **Supplementary Figs. 42-54**, the breakthrough times (from  $t_0$  to  $t_1$ ) were substantially reduced at higher flow rates, yet the desorption curves demonstrate that XXU-3a retains its excellent separation capability at higher flow rates. Specifically, the C<sub>3</sub>H<sub>6</sub> productivity and purity were estimated to be 34.2 L kg<sup>-1</sup> (99.5 %), 53.5 L kg<sup>-1</sup> (99.5 %), and 48.2 L kg<sup>-1</sup> (99.5 %) at flow rates of 1.0 mL min<sup>-1</sup>, 6.0 mL min<sup>-1</sup>, and 8.0 mL min<sup>-1</sup>, respectively (**Fig. 6**). Whereas the separation performance of KAUST-7 and Y-abtc did not significantly improve upon the increasing flow rates, their C<sub>3</sub>H<sub>6</sub> productivity and purity were estimated to be 21.0 L kg<sup>-1</sup> (90 %) and 3.76 L kg<sup>-1</sup> (90 %), respectively, at 8.0 mL min<sup>-1</sup> flow rate (**Fig. 6**).

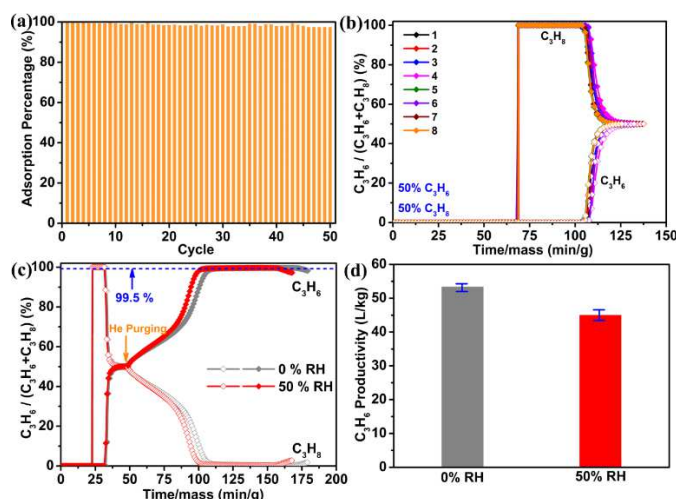


**Fig. 7. Recyclability and breakthrough experiment under humid conditions.** (a) C<sub>3</sub>H<sub>6</sub> adsorption on XXU-3a over 50 consecutive adsorption-desorption cycles in a single-component breakthrough experiment at 303 K; desorption was carried out by helium gas sweeping (10 mL min<sup>-1</sup>) for 15 min. (b) Eight breakthrough curves of XXU-3a for an equimolar C<sub>3</sub>H<sub>6</sub>/C<sub>3</sub>H<sub>8</sub> mixture at 303 K and 1 bar. (c) Breakthrough curves for an equimolar mixture of C<sub>3</sub>H<sub>6</sub>/C<sub>3</sub>H<sub>8</sub> at a flow rate of 6.0 mL min<sup>-1</sup> on XXU-3a under dry and humid conditions (50 % RH), followed by desorption curves under helium gas sweeping (10.0 mL min<sup>-1</sup>) at 303 K. (d) Comparison of C<sub>3</sub>H<sub>6</sub> productivity ( $\geq 99.5$  %) in volume per unit mass of adsorbents under 0% RH and 50 % RH conditions.

For practical industrial applications, the adsorbent should possess good recyclability. We carried out multiple dynamic breakthrough measurements for an equimolar C<sub>3</sub>H<sub>6</sub>/C<sub>3</sub>H<sub>8</sub> mixture on the same XXU-3a sample. In between measurements, the sample was regenerated under vacuum at room temperature. The recycling experiments reveal almost the same retention time for both C<sub>3</sub>H<sub>6</sub> and C<sub>3</sub>H<sub>8</sub> over eight continuous adsorption-desorption cycles (**Fig. 7b**), indicating no loss in C<sub>3</sub>H<sub>6</sub> adsorption capacity and C<sub>3</sub>H<sub>6</sub>/C<sub>3</sub>H<sub>8</sub> separation capacity. Further, continuous breakthrough experiments for pure C<sub>3</sub>H<sub>6</sub> were carried out with helium sweeping as a regeneration method. As shown in **Fig. 7a** and **Supplementary Fig. 55**, it was demonstrated that XXU-3a could be completely regenerated under helium sweeping, and no obvious loss of adsorption capacity after 50 cycles of C<sub>3</sub>H<sub>6</sub> adsorption-desorption. Additionally, dynamic column breakthrough experiments of an equimolar C<sub>3</sub>H<sub>6</sub>/C<sub>3</sub>H<sub>8</sub> mixture with a flow rate of 6.0 mL min<sup>-1</sup> were carried out on XXU-3a under either dry (0% RH) or humid conditions (50% RH) (**Fig. 7c**). The C<sub>3</sub>H<sub>6</sub> purity and productivity were estimated from their desorption curves (**Supplementary Fig. 57**). Under 50 % RH condition, 44.9 L of C<sub>3</sub>H<sub>6</sub> with over 99.5 % purity can be obtained from an equimolar C<sub>3</sub>H<sub>6</sub>/C<sub>3</sub>H<sub>8</sub> mixture for 1 kg of XXU-3a, which is lower than the productivity under 0% RH condition (53.3 L with over 99.5 % purity). The slight decrease in productivity is reasonable since the partial pressure of C<sub>3</sub>H<sub>6</sub> in the feed gas would be lowered upon the inclusion of water vapor, not to mention water vapor competing for adsorption sites. All the experiments were run three times and the averages were reported with small error bars (**Fig. 7d**).

## Outlook

The development of porous materials for efficient separation of C<sub>3</sub>H<sub>6</sub>/C<sub>3</sub>H<sub>8</sub> mixtures is of great importance, particularly the ones that can achieve polymer-grade C<sub>3</sub>H<sub>6</sub> production in a single adsorption-desorption operation. This work illustrated a MOF material (XXU-3) featuring 1D

channel with embedded molecular pockets opening to C<sub>3</sub>H<sub>6</sub> and C<sub>3</sub>H<sub>8</sub> at substantially different pressures, which was translated into efficient production of high-purity C<sub>3</sub>H<sub>6</sub> ( $\geq 99.95\%$ ) from an equimolar C<sub>3</sub>H<sub>6</sub>/C<sub>3</sub>H<sub>8</sub> mixture in a single adsorption-desorption. Furthermore, XXU-3 has demonstrated much higher productivity and at least one order of magnitude faster diffusion kinetics compared to the two best performing materials under similar conditions. The excellent separation performance of XXU-3a was attributed to the underlying separation mechanism, namely orthogonal-array dynamic molecular sieving. The structural design depicted here represents next-generation molecular sieving with the potential of achieving not only large separation capacity but also fast adsorption-desorption kinetics, both of which will have significant impacts on energy consumption in adsorptive separation. Besides, the dynamic nature may offer unusual separation capability which would otherwise difficult to realize. We anticipate the orthogonal-array dynamic molecular sieving strategy be extended to a broad scope of applications for efficient separation.

## Methods

### Materials

All reagents and solvents were obtained commercially and used as received without further purification. The ligand 5-(3-methyl-5-(pyridin-4-yl)-4*H*-1,2,4-triazol-4-yl)-1,3-benzenedicarboxylic acid (H<sub>2</sub>MPTBDC) was purchased from Shanghai Tensus Bio-tech Co., Ltd. Ultrahigh-purity-grade ( $>99.999\%$ ) Ar, C<sub>3</sub>H<sub>6</sub>, and C<sub>3</sub>H<sub>8</sub> gases were purchased from Dalian Special Gases CO., Ltd. Mixed gases C<sub>3</sub>H<sub>6</sub>/C<sub>3</sub>H<sub>8</sub> = 50/50 (mol/mol) was purchased from Huate Gas Co., Ltd.

### Scale-up synthesis of XXU-3

A mixture of Co(NO<sub>3</sub>)<sub>6</sub>·6H<sub>2</sub>O (5 mmol, 1.455 g), H<sub>2</sub>MPTBDC (5 mmol, 1.62 g), methanol (MeOH, 150 mL), and N,N-Dimethylacetamide (DMA, 150 mL) was placed in a sealed glass vial (500 mL) and heated at 120 °C for 12 h. After it was cooled to room temperature, the light purple crystals (as-synthesized XXU-3) were collected and washed with MeOH three times, then air-dried and heated under high vacuum at 150 °C for 24 h to afford desolvated XXU-3 (XXU-3a, ~ 2 g, ~ 65 % yield based on H<sub>2</sub>MPTBDC). Anal. calcd. (found) for (C<sub>16</sub>H<sub>10</sub>CoN<sub>4</sub>O<sub>4</sub>)·3H<sub>2</sub>O: C, 44.23 % (43.81 %); H, 3.69 % (3.94 %); N, 12.9 % (12.91 %).

### Gas adsorption measurement

At least 100 mg of sample was used for each measurement. XXU-3 was activated at 150 °C under a dynamic vacuum (below 5 μmHg) for 24 h. Single-component and mixed-component gas adsorption/desorption isotherms were measured on an ASAP 2020 PLUS Analyzer (Micromeritics). The time-dependent kinetic adsorption isotherms were collected on Micromeritics ASAP 2020 Plus in Rate of Adsorption (ROA) mode (place roa.exe in the directory where the 2020 Plus.exe is located).

### Powder X-ray diffraction (PXRD) analysis

Powder x-ray diffraction data were collected by using microcrystalline samples on a Rigaku Ultima IV diffractometer (40 kV, 40 mA, Cu K<sub>α1</sub>,  $2\lambda = 1.5418 \text{ \AA}$ ). The measurement parameters include a scan speed of 10 (°)/min, a step size of 0.02 (°), and a scan range of  $2\theta$  from 5 (°) to 30 (°). For

Temperature-dependent PXRD, the measurement parameters include a scan speed of 2 °C/min, a step size of 0.02 (°), and a scan range of  $2\theta$  from 5 (°) to 30 (°).

### **Single-crystal X-ray diffraction (SCXRD) analysis**

Gas-loaded XXU-3a was prepared by exposing XXU-3a crystal to corresponding gas at about 1 bar and room temperature for 3 h. Single crystal diffraction data of as-synthesized XXU-3 (150 K), XXU-3a (150 K, 298 K), C<sub>3</sub>H<sub>6</sub>@XXU-3a (150 K), and C<sub>3</sub>H<sub>8</sub>@XXU-3a (100 K) were collected *via* an Oxford Cryo stream system on a XtaLAB PRO MM007-DW diffractometer system equipped with a RA-Micro7HF-MR-DW (Cu/Mo) X-ray generator and HyPix-6000HE Hybrid Photon Counting (HPC) X-ray detector (Rigaku, Japan, Cu K $\alpha$ ,  $2\lambda = 1.54178 \text{ \AA}$ ). The structures were solved and refined using Olex 2 with 'XS' and 'XL' plug-ins.

### **Column breakthrough experiments**

The mixed-gas breakthrough separation experiment was conducted under ambient conditions (303 K, 1 atm) by using an in-house assembled system. XXU-3a powder (1.4 g) was packed into a custom-made stainless-steel column (3.15 mm, I.D.  $\times$  450 mm) with silica wool filling the void space. The sorbent was activated *in-situ* in the column at 373 K with a high vacuum for 12 h and helium was introduced to saturate the column before breakthrough experiment.

### **Competing interests**

The authors declare no competing interests.

## References

1. IHS, Natural Gas Liquids Challenging Oil as Petrochemical Feedstock in North America, Increasing Global Demand for On-Purpose Production of Propylene (2014).
2. Eldridge, R.B. Olefin/paraffin separation technology: a review. *Ind. Eng. Chem. Res.* **32**, 2208-2212 (1993).
3. Sholl, D. S., Lively, R. P. Seven chemical separations to change the world. *Nature* **532**, 435-437 (2016).
4. Li, J.-R., Kuppler, R. J., Zhou, H.-C. Selective gas adsorption and separation in metal-organic frameworks. *Chem. Soc. Rev.* **45**, 1477-1504 (2009).
5. Rege, S. U., Yang, R. T. Propane/propylene separation by pressure swing adsorption: sorbent comparison and multiplicity of cyclic steady states, *Chem. Eng. Sci.* **57**, 1139 (2002).
6. Papastathopoulou, H. S., Luyben, W. L. Control of a binary sidestream distillation column, *Ind. Eng. Chem. Res.* **30**, 705-713 (1991).
7. Martins, V. F. D., Ribeiro, A. M., Santos, J. C. et al. Development of Gas Phase SMB Technology for Light Olefin/Paraffin Separations Vanessa. *AIChE J.* **62**, 2490-2500 (2016).
8. Narin, G., Martins, V. F. D., Campo, M. et al. Light olefins/paraffins separation with 13X zeolite binderless beads. *Sep. Purif. Technol.* **133**, 452-475 (2014).
9. Chai, Y., Han, X., Li, W. et al. Control of zeolite pore interior for chemoselective alkyne/olefin separations. *Science* **368**, 1002-1006 (2020).
10. Zhou, H. C.; Long, J. R.; Yaghi, O. M. Introduction to metal organic frameworks. *Chem. Rev.* **112**, 673-674 (2012).
11. Zhou, H. C., Kitagawa, S. Metal-organic frameworks (MOFs). *Chem. Soc. Rev.* **43**, 5415-5418 (2014).
12. Furukawa, H., Cordova, K. E., O’Keeffe, M., Yaghi, O. M. The chemistry and applications of metal-organic frameworks. *Science* **341**, 1230444 (2013).
13. Chen, B., Xiang, S. C., Qian, G. D. Metal-organic frameworks with functional pores for recognition of small molecules. *Acc. Chem. Res.* **43**, 1115-1124 (2010).
14. Cho, H. S., Yang, J., Gong, X., Zhang, Y.-B., Momma, K., Weckhuysen, B. M., Deng, H., Kang, J. K., Yaghi, O. M., Terasaki, O. Isotherms of Individual Pores by Gas Adsorption Crystallography. *Nat. Chem.* **11**, 562-570 (2019).
15. Yaghi, O. M., Kalmutzki, M. J., Diercks, C. S. Introduction to Reticular Chemistry: Metal-Organic Frameworks and Covalent Organic Frameworks; Wiley-VCH: Weinheim, 2019.
16. Cadiau, A., Adil, K., Bhatt, P. M., Belmabkhout, Y., Eddaoudi, M. A metal-organic framework-based splitter for separating propylene from propane, *Science* **353**, 137-140 (2016).
17. Wang, H., Dong, X., Colombo, V. et al. Tailor-Made Microporous Metal-Organic Frameworks for the Full Separation of Propane from Propylene Through Selective Size

- Exclusion. *Adv. Mater.* **30**, 1805088 (2018).
18. Bachman, J. E., Kapelewski, M. T., Reed, D. A. et al. M(*m*-dobdc) (M = Mn, Fe, Co, Ni) Metal-organic frameworks as highly selective, high-capacity adsorbents for olefin/paraffin separations. *J. Am. Chem. Soc.* **139**, 15363-15370 (2017).
  19. Bloch, E. D., Queen, W. L., Krishna, R. et al. Hydrocarbon separations in a metal-organic framework with open iron(II) coordination sites, *Science* **335**, 1606-1610 (2012).
  20. Lin, R., Li, L., Zhou, H. et al. Molecular sieving of ethylene from ethane using a rigid metal-organic framework. *Nat. Mater.* **17**, 1128-1133 (2018).
  21. Ye, Y., Ma, Z., Lin, R-B. et al. Pore Space Partition within a Metal-Organic Framework for Highly Efficient C<sub>2</sub>H<sub>2</sub>/CO<sub>2</sub> Separation. *J. Am. Chem. Soc.* **141**, 9, 4130-4136 (2019).
  22. Pei, J., Shao, K., Wang, J-X. et al. A Chemically Stable Hofmann-Type Metal-Organic Framework with Sandwich-Like Binding Sites for Benchmark Acetylene Capture. *Adv. Mater.* **32**, 1908275 (2020).
  23. Smith, G. L., Eyley, J. E., Han, Xue. et al. Reversible coordinative binding and separation of sulfur dioxide in a robust metal-organic framework with open copper sites. *Nat. Mater.* **18**, 1358-1365 (2019).
  24. Chen, K-J., Madden, D., Mukherjee, S. et al. Synergistic sorbent separation for one-step ethylene purification from a four-component mixture. *Science* **366**, 241-246 (2019).
  25. Peng, Y-L., He, C., Pham, T. et al. Robust Microporous Metal-Organic Frameworks for Highly Efficient and Simultaneous Removal of Propyne and Propadiene from Propylene. *Angew. Chem. Int. Ed.* **58**, 10209-10214 (2019).
  26. Yang, X., Zhou, H-L., He, C-T. et al. Flexibility of Metal-Organic Framework Tunable by Crystal Size at the Micrometer to Submillimeter Scale for Efficient Xylene Isomer Separation. *Research* 9463719 (2019).
  27. Mohanty, S., McCormick, A. V. Prospects for principles of size and shape selective separations using zeolites. *Chem. Eng. J.* **74**, 1-14 (1999).
  28. Nugent, P., Belmabkhout, Y., Burd, S. D. et al. Porous materials with optimal adsorption thermodynamics and kinetics for CO<sub>2</sub> separation. *Nature* **495**, 80-84 (2013).
  29. Li, B., Cui, X., O'Nolan, D. et al. An Ideal Molecular Sieve for Acetylene Removal from Ethylene with Record Selectivity and Productivity. *Adv. Mater.* **29**, 1704210 (2017).
  30. Hu, T., Wang, H., Li, B. et al. Microporous metal-organic framework with dual functionalities for highly efficient removal of acetylene from ethylene/acetylene mixtures. *Nat Commun* **6**, 7328 (2015).
  31. Zhou, D., Chen, P., Wang, C. et al. Intermediate-sized molecular sieving of styrene from larger and smaller analogues. *Nat. Mater.* **18**, 994-998 (2019).
  32. Ma, S., Sun, D., Wang, X.-S. & Zhou, H.-C. A mesh-adjustable molecular sieve for general use in gas separation. *Angew. Chem. Int. Ed.* **46**, 2458-2462 (2007).

33. Katsoulidis, A.P., Antypov, D., Whitehead, G.F.S. et al. Chemical control of structure and guest uptake by a conformationally mobile porous material. *Nature* **565**, 213-217 (2019).
34. Gu, C. et al. Design and control of gas diffusion process in a nanoporous soft crystal. *Science* **363**, 387-391 (2019).
35. Krokidas, P., Castier, M., Moncho, S. et al. Molecular Simulation Studies of the Diffusion of Methane, Ethane, Propane, and Propylene in ZIF-8. *J. Phys. Chem. C* **119**, 27028-27037 (2015).
36. Ferey, G., Serre, C. Large breathing effects in three-dimensional porous hybrid matter: facts, analyses, rules and consequences. *Chem. Soc. Rev.* **38**, 1380-1399 (2009).
37. Lin, R. B., Li, L., Wu, H. et al. Optimized separation of acetylene from carbon dioxide and ethylene in a microporous material. *J. Am. Chem. Soc.* **139**, 8022-8028 (2017).
38. Li, L., Lin, R.B., Krishna, R. et al. Flexible robust metal-organic framework for efficient removal of propyne from propylene, *J. Am. Chem. Soc.* **139**, 7733-7736 (2017).
39. Wang, X., Krishn, R., Li, L. et al. Guest-dependent pressure induced gate-opening effect enables effective separation of propene and propane in a flexible MOF. *Chem. Eng. J.* **346**, 489-496 (2018).
40. Grande, C. A., Rodrigues, A. E. Adsorption kinetics of propane and propylene in zeolite 4A. *Chem. Eng. Res. Des.* **82**, 1604-1624 (2004).
41. Khalighi, M., Karimi, I. A., Farooq, S. Comparing SiCHA and 4A Zeolite for Propylene/Propane Separation using a Surrogate-Based Simulation/Optimization Approach. *Ind. Eng. Chem. Res.* **53**, 16973-16983 (2014).
42. Liang, B. et al. An Ultramicroporous Metal-Organic Framework for High Sieving Separation of Propylene from Propane. *J. Am. Chem. Soc.* **142**, 17795-17801 (2020).
43. Klet, R. C. et al. Single-site organozirconium catalyst embedded in a metal-organic framework. *J. Am. Chem. Soc.* **137**, 15680-15683 (2015).
44. Myers, A. L., Prausnitz, J. M. Thermodynamics of mixed-gas adsorption. *AIChE J.* **11**, 121 (1965).
45. Lee, C. Y., Bae, Y-S., Jeong, N. C. et al. Kinetic Separation of Propene and Propane in Metal Organic Frameworks: Controlling Diffusion Rates in Plate-Shaped Crystals *via* Tuning of Pore Apertures and Crystallite Aspect Ratios. *J. Am. Chem. Soc.* **133**, 5228-5231 (2011).
46. Grimme, S. Semiempirical GGA-type density functional constructed with a long-range dispersion correction. *J. Chem. Phys.* **124**, 152201 (2006).
47. R. A. Meyers, Handbook of Petrochemicals Production Processes (McGraw-Hill, 2005).

# Figures

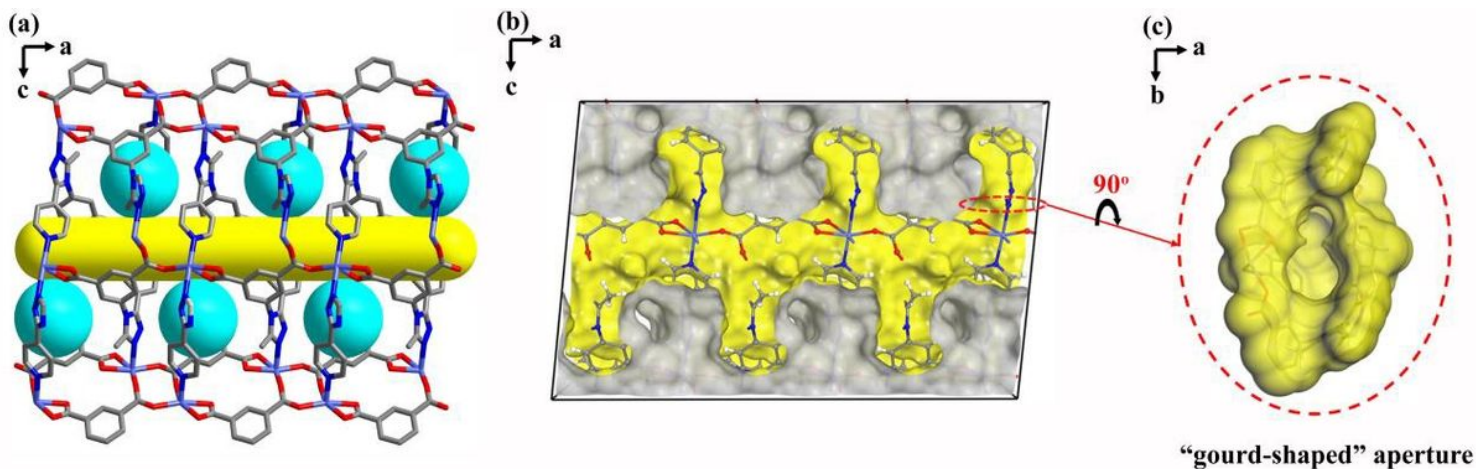


Figure 1

Crystal structure of XXU-3. (a) Pore structure viewed along the b axis showing molecular pockets (turquoise) and one-dimension channel (yellow). (b) Cross-sectional view of Connolly surface of the void in (a), where a probe radius of 0.8 Å was used to visualize the molecular pockets opening to the one-dimension channel. (c) Close-up view of the "gourd-shaped" aperture connecting the pocket to the channel. Color code: light blue, Co; red, O; blue, N; white, H; grey, C atoms. H atom is omitted in (a) for clarity.

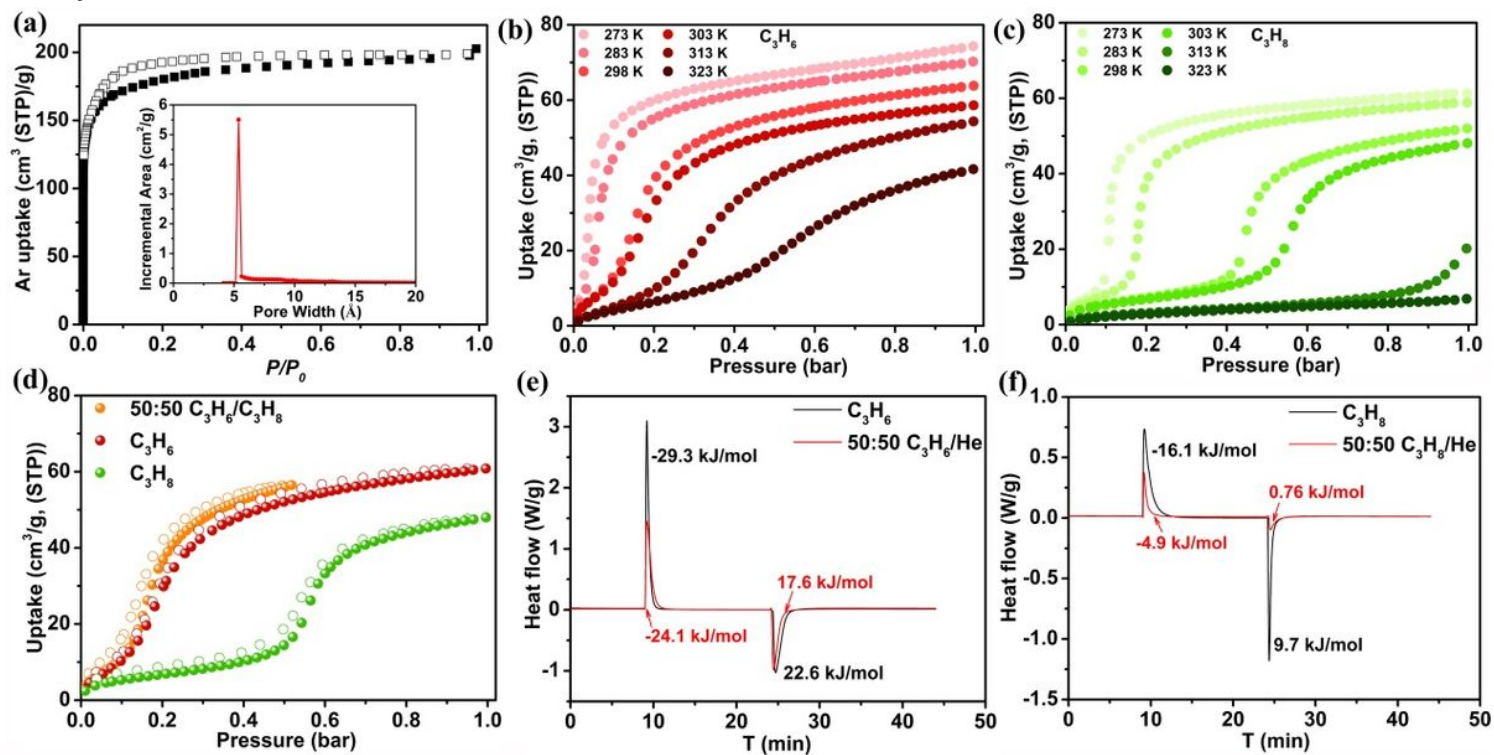


Figure 2

Gas sorption properties and DSC profiles. (a) Low-pressure Ar adsorption/desorption isotherms of XXU-3a at 87 K. (inset) calculated pore-size distribution of XXU-3a based on the adsorption branch. (b) C<sub>3</sub>H<sub>6</sub> adsorption isotherms of XXU-3a at different temperatures. (c) C<sub>3</sub>H<sub>8</sub> adsorption isotherms of XXU-3a at different temperatures. (d) Pure C<sub>3</sub>H<sub>8</sub> (green), pure C<sub>3</sub>H<sub>6</sub> (red), and an equimolar mixture of C<sub>3</sub>H<sub>6</sub>/C<sub>3</sub>H<sub>8</sub> (orange) adsorption/desorption isotherms of XXU-3a at 303 K. For the equimolar mixture, the x-axis is partial pressure of C<sub>3</sub>H<sub>6</sub>. (e) Differential scanning calorimetry of C<sub>3</sub>H<sub>6</sub> and 50/50 C<sub>3</sub>H<sub>6</sub>/He adsorption and desorption on XXU-3a at 303 K and 1 bar. (f) Differential scanning calorimetry of C<sub>3</sub>H<sub>8</sub> and 50/50 C<sub>3</sub>H<sub>8</sub>/He adsorption and desorption on XXU-3a at 303 K and 1 bar. In (e) and (f), the adsorption was carried out under C<sub>3</sub>H<sub>6</sub>, C<sub>3</sub>H<sub>8</sub>, or 50/50 mixed-component (C<sub>3</sub>H<sub>6</sub>/He and C<sub>3</sub>H<sub>8</sub>/He) at a flow rate of 5.0 mL min<sup>-1</sup>. The desorption was carried out under helium at a flow rate of 5.0 mL min<sup>-1</sup> starting at 15-min time point.

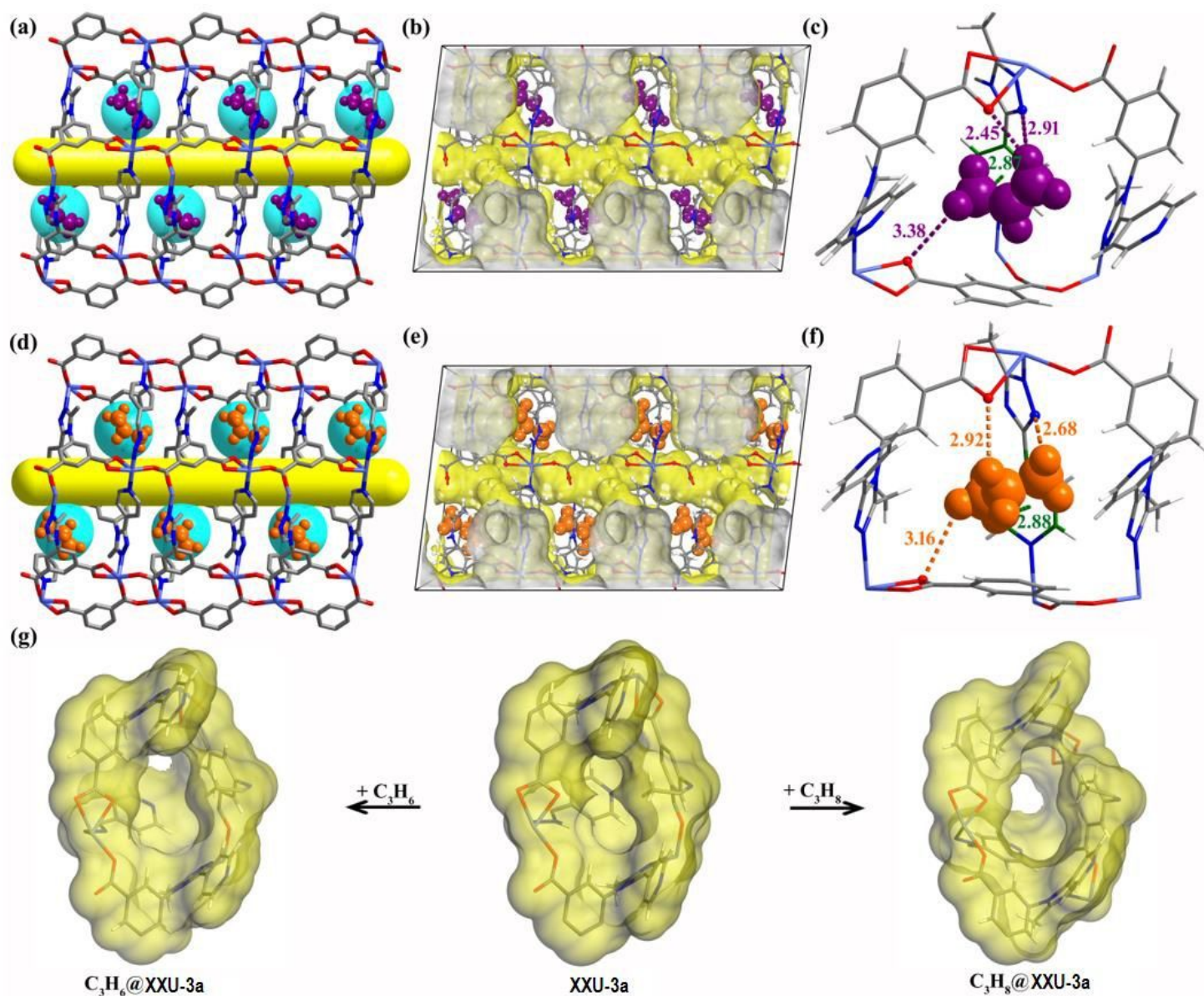
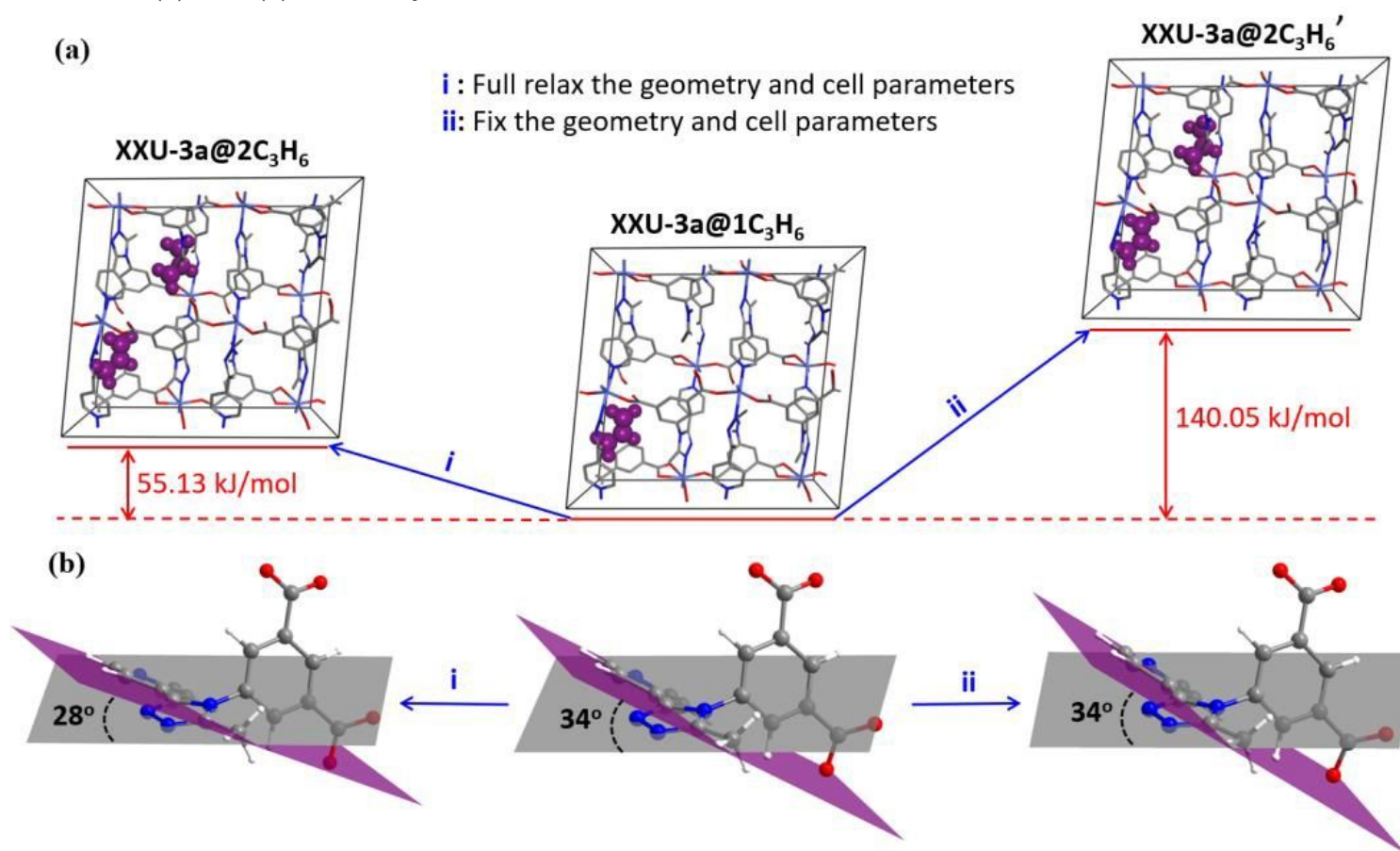


Figure 3

Binding sites and dynamic gate-opening. (a) Crystal structure of C<sub>3</sub>H<sub>6</sub>@XXU-3a viewed along the b axis highlighting the pocket-occupying C<sub>3</sub>H<sub>6</sub> molecules. (b) Connolly surface representation of C<sub>3</sub>H<sub>6</sub>@XXU-3a along the b axis with the adsorbed C<sub>3</sub>H<sub>6</sub> molecules. (c) Close-up view of C<sub>3</sub>H<sub>6</sub> in the single crystal of C<sub>3</sub>H<sub>6</sub>@XXU-3a, showing multiple interactions with surrounding linkers on the pocket. C<sub>3</sub>H<sub>6</sub> molecules are shown in a space-filling model depicted in violet, and distances are in Å. (d) Crystal structure of C<sub>3</sub>H<sub>8</sub>@XXU-3a viewed along the b axis highlighting the pocket-occupying C<sub>3</sub>H<sub>8</sub> molecules. (e) Connolly surface representation of C<sub>3</sub>H<sub>8</sub>@XXU-3a along the b axis with the adsorbed C<sub>3</sub>H<sub>8</sub> molecules. (f) Close-up view of C<sub>3</sub>H<sub>8</sub> in the single crystal of C<sub>3</sub>H<sub>8</sub>@XXU-3a, showing multiple interactions with surrounding organic linkers on the pocket, C<sub>3</sub>H<sub>8</sub> molecules are shown in a space-filling model depicted in orange, and distances are in Å. (g) Connolly surface comparison to illustrate the opening up of the “gourd-shaped” aperture along with the adsorption of C<sub>3</sub>H<sub>6</sub> or C<sub>3</sub>H<sub>8</sub>. C<sub>3</sub>H<sub>8</sub> and C<sub>3</sub>H<sub>6</sub> were omitted for clarity. Color code: light blue, red, blue, white, and grey nodes represent Co, O, N, H, and C atoms, respectively. H atom is omitted in (a) and (d) for clarity.



**Figure 4**

DFT calculations. (a) Geometry optimization by density functional theory (DFT) for (i) XXU-3a@2C<sub>3</sub>H<sub>6</sub>, full relax the geometry and cell parameters; and (ii) XXU-3a@2C<sub>3</sub>H<sub>6</sub>', fix the geometry and cell parameters. (b) The rotation of the dihedral angle of the pyridine plane and triazole plane. Color code: light blue, red, blue, white, and grey represent Co, O, N, H, and C atoms, respectively. H atom is omitted in (a) for clarity.

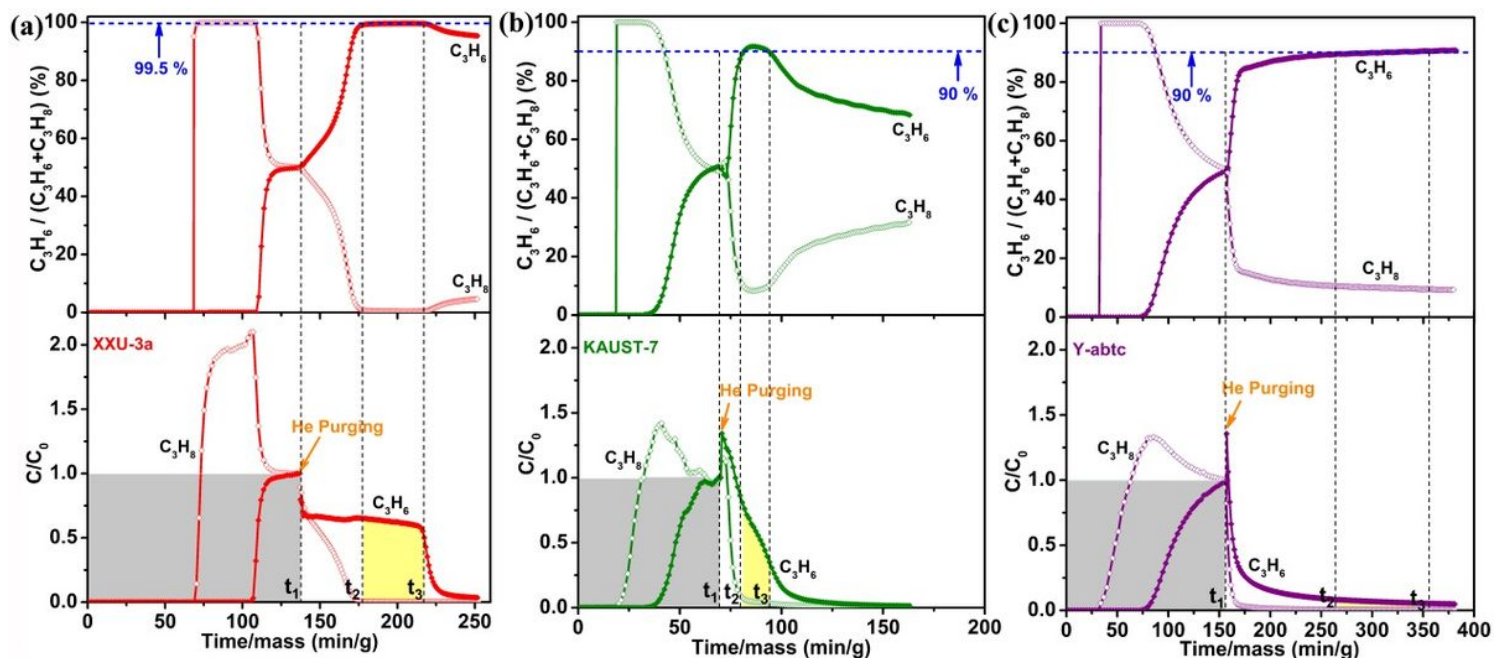


**Figure 5**

Breakthrough experiments. Breakthrough curves of an equimolar mixture of C<sub>3</sub>H<sub>6</sub>/C<sub>3</sub>H<sub>8</sub> (1.0 mL min<sup>-1</sup>) on XXU-3a, KAUST-7, and Y-abtc, followed by desorption curves under helium gas (10.0 mL min<sup>-1</sup>) sweeping at 303 K. C<sub>3</sub>H<sub>8</sub> (open diamonds), C<sub>3</sub>H<sub>6</sub> (solid diamonds). For comparison, the x-axis is normalized to “time per gram adsorbents”. C and C<sub>0</sub> are the concentrations of each gas at the outlet and inlet, respectively. Dashed blue lines highlight the gas composition at 99.5 % and 90 %, respectively. Grey area: mixed gas input. Yellow area: C<sub>3</sub>H<sub>6</sub> gas output.

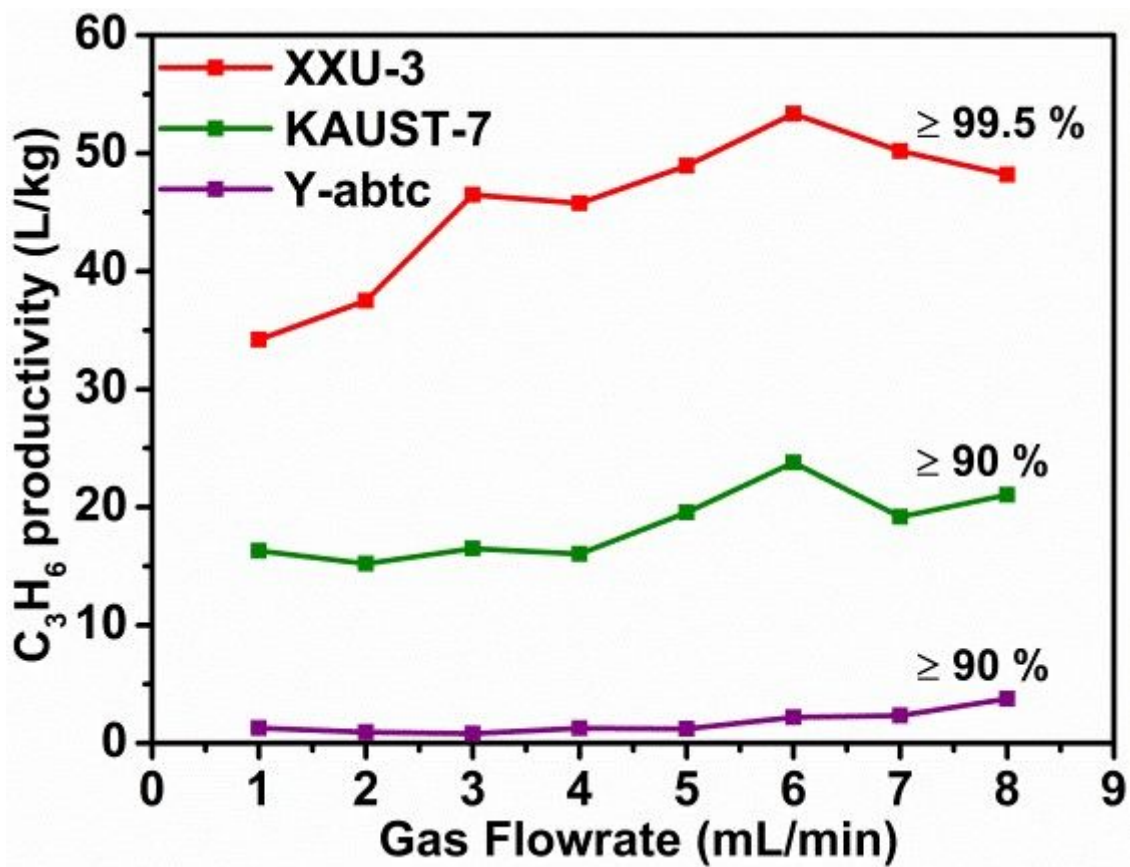


Figure 6

C<sub>3</sub>H<sub>6</sub> productivity and purity. Comparison of C<sub>3</sub>H<sub>6</sub> productivity and purity estimated from the experimental breakthrough data of an equimolar C<sub>3</sub>H<sub>6</sub>/C<sub>3</sub>H<sub>8</sub> mixture on XXU-3a, KAUST-7, and Y-abtc at different flowrates.

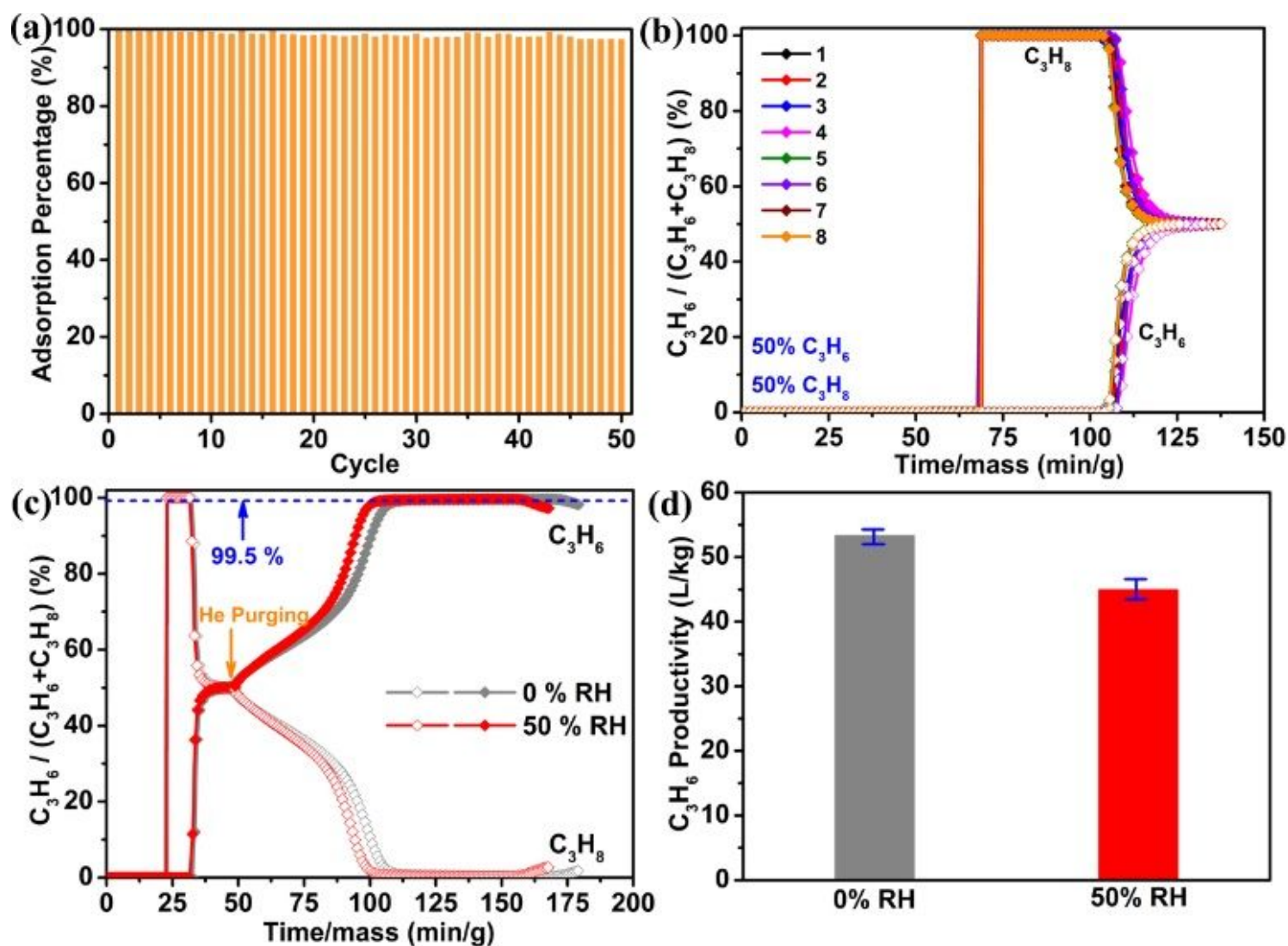


Figure 7

Recyclability and breakthrough experiment under humid conditions. (a)  $C_3H_6$  adsorption on XXU-3a over 50 consecutive adsorption-desorption cycles in a single-component breakthrough experiment at 303 K; desorption was carried out by helium gas sweeping ( $10 \text{ mL min}^{-1}$ ) for 15 min. (b) Eight breakthrough curves of XXU-3a for an equimolar  $C_3H_6/C_3H_8$  mixture at 303 K and 1 bar. (c) Breakthrough curves for an equimolar mixture of  $C_3H_6/C_3H_8$  at a flow rate of  $6.0 \text{ mL min}^{-1}$  on XXU-3a under dry and humid conditions (50 % RH), followed by desorption curves under helium gas sweeping ( $10.0 \text{ mL min}^{-1}$ ) at 303 K. (d) comparison of  $C_3H_6$  productivity (99.5 %) in volume per unit mass of adsorbents under 0% RH and 50 % RH conditions.

## Supplementary Files

This is a list of supplementary files associated with this preprint. Click to download.

- [SupplementaryInformationDB.pdf](#)